

## Azimuthal anisotropy of longwave and infrared window radiances from the Clouds and the Earth's Radiant Energy System on the Tropical Rainfall Measuring Mission and Terra satellites

Patrick Minnis

Atmospheric Sciences, NASA Langley Research Center, Hampton, Virginia, USA

Arvind V. Gambheer and David R. Doelling

Analytical Services and Materials, Inc., Hampton, Virginia, USA

Received 19 December 2003; revised 1 March 2004; accepted 11 March 2004; published 16 April 2004.

[1] Shadowing by vegetation, landforms, or clouds can reduce the surface temperature relative to unshadowed portions of the same land area. This shading effect can cause azimuthal variation of the outgoing infrared radiance that is currently not taken into account in remote sensing and Earth radiation budget analyses. In this paper, multiangle longwave (LW) (5–200  $\mu\text{m}$ ) and window (WN) (8–12  $\mu\text{m}$ ) radiances taken by the Clouds and the Earth's Radiant Energy System (CERES) rotating azimuth plane scanner on the Tropical Rainfall Measuring Mission (TRMM) and Terra satellites are used to determine the azimuthal anisotropy of LW and WN fields over all solar zenith angles and surface types in clear and cloudy conditions. The azimuthal component of the anisotropy is isolated by constructing limb-darkening models for each category of surface type and topography in each solar zenith angle (SZA) bin. The viewing zenith angle dependence of WN and LW radiances in clear scenes depends on the SZA, possibly because of changes in the boundary layer temperature structure during the day. The observed mean radiances, in general, are greater when viewing the sunlit hemisphere (backscattering) than when viewing the shaded (forward scattering) hemisphere. This forward-back contrast increases with increasing terrain roughness and is stronger for surfaces with open vegetation such as shrubs and grass than for contiguous vegetation like forests. The anisotropy is less well defined for barren deserts. Maximum anisotropy occurs for SZAs between  $48^\circ$  and  $70^\circ$ . This paper provides the first evidence that clouds also induce longwave azimuthal anisotropy. Strong forward-back radiance contrast is evident for partly, mostly, and overcast scenes for  $\text{SZA} < 48^\circ$ . The contrast disappears for overcast scenes and decreases for partly and mostly cloudy scenes at higher SZAs. The TRMM sampling is limited and causes some biases at particular angle sets but overall provides a reasonable depiction of the anisotropy at all SZAs. Terra yields a more accurate anisotropy characterization but only for SZAs between  $48^\circ$  and  $70^\circ$ . A simple model constructed from the TRMM results for clear scenes reduces clear-sky temperature prediction RMS errors by 38% or more while minimizing the biases associated with azimuthal anisotropy. The model should yield similar or better reductions in the errors associated with retrievals of skin temperature or LW fluxes, especially those from geostationary satellites. In addition, future analyses of combined TRMM, Terra, and Aqua CERES data will likely provide more accurate correction models that could further reduce errors in surface skin temperature and radiative flux for both clear and cloudy scenes.

*INDEX TERMS:* 3360 Meteorology and Atmospheric Dynamics: Remote sensing; 3359 Meteorology and Atmospheric Dynamics: Radiative processes; 3307 Meteorology and Atmospheric Dynamics: Boundary layer processes; 3314 Meteorology and Atmospheric Dynamics: Convective processes; 1640 Global Change: Remote sensing;  
*KEYWORDS:* infrared radiation, surface temperature, remote sensing

**Citation:** Minnis, P., A. V. Gambheer, and D. R. Doelling (2004), Azimuthal anisotropy of longwave and infrared window radiances from the Clouds and the Earth's Radiant Energy System on the Tropical Rainfall Measuring Mission and Terra satellites, *J. Geophys. Res.*, 109, D08202, doi:10.1029/2003JD004471.

## 1. Introduction

[2] Accurate estimates of the Earth radiation budget and the surface skin temperature are becoming increasingly important for climate [Wielicki *et al.*, 1996] and weather prediction [e.g., Garand, 2003], respectively. Such estimates are generally based on measurements of broadband or narrowband radiances that provide only one perspective of the viewed scene. This limited perspective can bias the estimate of flux or skin temperature because of anisotropy in the radiance field. Anisotropy arises because of the optical properties and three-dimensional structure of natural surfaces and the effects of the intervening atmosphere. The three-dimensional anisotropy of reflected shortwave radiation has long been recognized [e.g., Coulson *et al.*, 1965] and a host of anisotropic directional models [e.g., Suttles *et al.*, 1988; Loeb *et al.*, 2003] have been developed to account for it. For the most part, the anisotropy of radiation emitted by the Earth-atmosphere system has been considered as a one-dimensional problem that can be addressed with a limb-darkening model (LDM) to account for the average variation of outgoing thermal radiation with the viewing zenith angle (VZA). Typically, LDMs implicitly or explicitly account for the combined effects of atmospheric absorption and re-emission [e.g., Minnis and Harrison, 1984] and surface emissivity as functions of scene type [e.g., Suttles *et al.*, 1989; Prata, 1993]. More recently, Loeb *et al.* [2003] developed a greatly improved set of empirical LDMs by accounting for the effects of variations in cloud phase, optical thickness, and atmosphere in addition to surface type and degree of cloudiness. These new LDMs greatly reduce the average error in the longwave (LW) flux at the top of the atmosphere (TOA) over a given location, especially when measured by nongeostationary satellites. However, they only account for the VZA dependence of thermal radiation, and the resulting instantaneous flux or skin temperature may have relatively large errors over land surfaces.

[3] Several studies [e.g., Kimes and Kirchner, 1983; Paw *et al.*, 1989] have demonstrated that, over land surfaces, thermal emission is a three-dimensional problem due to differential heating of the surface as a result of shadowing. Thus the relative azimuth (RAA) and solar zenith (SZA) angles must be considered when interpreting thermal radiances observed over land surfaces. The importance of the RAA can be visualized from Figure 1 that shows a schematic diagram of a satellite radiance measurement during daytime. Logically, a measurement of infrared (IR) radiance from the satellite position should produce a lower value than one from, say, the solar position because the shadowed area would be cooler than the illuminated area.

[4] Using limited matched geostationary satellite imager data, Minnis and Khaiyer [2000] showed that shadowing effects over land cause azimuthal variations of IR brightness temperatures that would affect large-scale daytime estimates of surface temperature  $T_s$  and the TOA LW flux. They concluded that variations in local topography, either landforms or vegetation, can cause these azimuthal variations and that the patterns vary with SZA or time of the day. They found a high correlation between bidirectional reflectance anisotropy and the angular variation of  $T_s$  that depends on terrain variability. Their results showed instantaneous errors

of up to  $15 \text{ W m}^{-2}$  and  $4^\circ\text{C}$  in LW flux and  $T_s$ , respectively, but were limited to narrowband IR measurements from pairs of angles over a range of local times at several locations. A complete characterization of the 3-D variation of  $T_s$  and the LW radiance would require measurements over all times of day from all angles at a given location or, at least, for a given surface type.

[5] Prior to implementation of the Clouds and the Earth's Radiant Energy System [CERES; Wielicki *et al.*, 1998], it had not been possible to take sufficient measurements to accurately depict the azimuthal anisotropy of either LW flux or  $T_s$ . Because of their unique characteristics, the CERES data taken from the Tropical Rainfall Measuring Mission (TRMM), Terra, and Aqua satellites can be used to advance our knowledge of the azimuthal dependence of thermal infrared radiation exiting the TOA. In this study, the CERES data are used to develop statistics of the azimuthal variation of both IR window and LW radiances for various surface and terrain types for all times of day over the tropics and subtropics. Additionally, the potential impact of clouds on the anisotropy is examined for the first time. These statistics are used to construct a simple model that can be used to reduce the instantaneous errors in the derived LW flux or skin temperature or to predict the temperature or radiance that would be viewed in a given direction.

## 2. Data

[6] TRMM is a precessing satellite in a circular orbit at 350 km with a  $35^\circ$  inclination giving it a 48-day repeat cycle. The TRMM CERES scanner has a spatial resolution of about 10 km at nadir and scans to the limb with a VZA limit of approximately  $70^\circ$  yielding coverage between about  $38^\circ\text{S}$  and  $38^\circ\text{N}$ . It measures reflected shortwave (SW;  $0.3\text{--}5 \mu\text{m}$ ) radiance, infrared window (WN;  $8\text{--}12 \mu\text{m}$ ) radiance  $L_{wn}$ , and the total radiance ( $0.3\text{--}200 \mu\text{m}$ ), which is the combined reflected and emitted radiation from the viewed scene. The raw radiances are unfiltered to account for the spectral response characteristics of the sensor. The LW ( $5\text{--}200 \mu\text{m}$ ) radiance  $L_{lw}$  is obtained by subtracting the unfiltered SW radiance from the unfiltered total radiance. Nominally, the scanner operates in an alternating pattern switching mode between 2 days of cross-track scanning followed by 1 day in the rotating azimuth plane scan (RAPS) mode. In that mode, the scanner continues operating in a cross-track action but it moves in a circular fashion as it scans back and forth. The RAPS mode has the potential for observing a given region from one or more VZA and RAA combinations during a given overpass, but its data are most useful for building up statistics of radiances at a particular pair of VZAs and RAAs. Data from the TRMM CERES scanner were taken continuously from January through August 1998 and during the entire month of March 2000. However, the RAPS mode was occasionally preempted to operate in a different mode.

[7] The CERES Single Scanner Footprint TOA/Surface and Clouds (SSF) TRMM edition 2B, Terra edition 1A, and Aqua Beta 1 RAPS LW and WN radiances are used here to examine the 3-D anisotropy in emitted radiation. The SSF data combine the CERES radiances with cloud properties [Minnis *et al.*, 2002a, 2003] convolved into the CERES

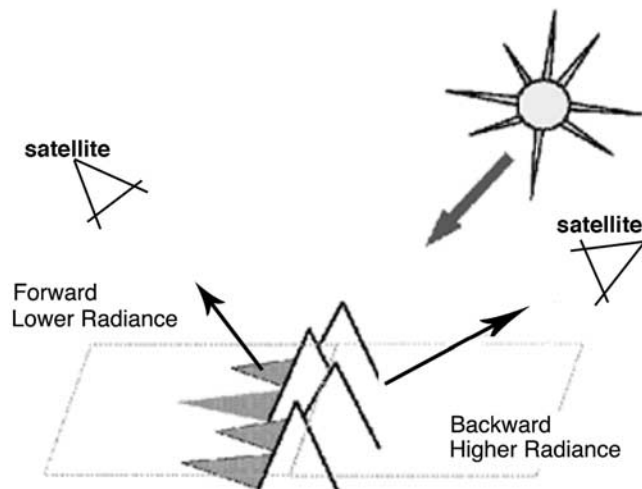


**Figure 1.** Schematic of satellite-Sun configuration with shadowing and relative infrared radiance emission.

scanner footprint [Wielicki *et al.*, 1998]. The cloud properties, which include cloud phase, height, optical depth and other parameters, were derived from the TRMM Visible Infrared Scanner (VIRS), which has a nominal resolution of 2 km, and from the Moderate Resolution Imaging Spectroradiometer (MODIS) on Terra and Aqua. The 1-km MODIS data were sampled to an effective resolution of 2 km. Only the cloud fraction  $Ac$  for each SSF is considered here. The VIRS is a cross-track scanner that has a maximum VZA of approximately  $48^\circ$  providing coverage between  $37^\circ\text{S}$  and  $37^\circ\text{N}$ . Development of anisotropic models from data taken over different regions implicitly assumes that there is an equal chance to measure radiances from all available scattering angles from any location. Because of the TRMM orbit configuration, nearly all of the CERES data viewing poleward of  $33^\circ\text{N}$  are observed in the backscattering hemisphere. Thus only data taken equatorward of  $33^\circ$  latitude were used here to prevent biases from views poleward of  $33^\circ$ . When the CERES operates in the RAPS mode, the cloud information and radiances come from two different viewing perspectives. The VIRS scanning angle limits the angular coverage by the SSF, so that some CERES RAPS data with VZA between  $48^\circ$  and  $70^\circ$  are not used because they have no matching VIRS cloud properties. This data set is the same as that analyzed by Loeb *et al.* [2003]. The MODIS scans out to a VZA of  $\sim 70^\circ$  so that the cloud data are available for all of the CERES footprints.

[8] The TRMM orbit yields sampling of all local times in a given area over 48 days providing measurements with complete diurnal coverage. The SSF data were available for a total of 269 days between January and August 1998. Only 68 actual RAPS SSFs were available during this period because the scanner was used in either an along- or cross-track mode instead of the RAPS mode (see Loeb *et al.* [2003] for details). Because of the limited operation of the RAPS and the sampling at different times of day, the sampling is somewhat diluted for certain conditions and SZAs. For a given  $1^\circ$  region, typically fewer than 40 clear CERES pixels were obtained over the 68 days in a specific angular bin (defined in section 3). Those pixels generally

correspond to measurements taken during 3 or 4 different days over the period. Better sampling was available over the desert areas of northern Africa and western Asia.

[9] To obtain better sampling at particular SZAs and ensure that the TRMM data are representative, CERES RAPS data taken between  $60^\circ\text{N}$  and  $60^\circ\text{S}$  from Terra [Minnis *et al.*, 2002a] and Aqua are also analyzed. Terra and Aqua are in Sun-synchronous orbits with nominal equatorial crossing times of 1030 and 1330 local time (LT), respectively. Both satellites sample very similar, but small ranges of SZA for a given latitude band during a given season. Terra data taken during 753 days between March 2000 and August 2002 and Aqua data taken during January 2003 are used here.

[10] Geostationary satellite infrared (IR;  $\sim 11 \mu\text{m}$ ) data and averaged VIRS radiances are used to test the model developed here. The geostationary data considered here consist of spectral radiances taken every 3 hours during 1998 from Meteosat-6, the eighth Geostationary Operational Environmental Satellite (GOES-8), and the fifth Geostationary Meteorological Satellite (GMS-5). These data were averaged on a regular  $1^\circ$  latitude-longitude grid as part of the CERES internal Temporal Interpolation Spatial Averaging (TISA) Gridded Geostationary Orbits (GGEO) Narrow-band Radiances data set. The VIRS spectral radiances and cloud products were also averaged on the same  $1^\circ$  grid as part of the TISA monthly gridded top of atmosphere (TOA)/surface fluxes and clouds (SFC) data set. Hereafter,  $1^\circ$ -gridded VIRS and geostationary satellite mean infrared radiances are referred to as SFC or VIRS, and GGEO data, respectively.

[11] Terrain variability is based on the ETOPO5 surface elevation data set [NOAA, 1988], a digital database of land and seafloor elevations on a  $5'$  latitude-longitude grid ( $\sim 10 \text{ km}$ ) with a nominal 1-m vertical resolution. For each  $5'$  region, the surface variability (SV) is defined as the standard deviation of the surface elevation computed using the altitudes from the subject region and the 8 adjacent regions. The resulting value of SV is used to determine the index for grouping the region into one of three topographical bins for each surface type. The first topography bin, the minimum surface variability bin, contains all regions with SV in the lowest 40 percentiles of surface variability. The next bin, medium, uses the terrain variability percentiles between 40 and 70. The remaining data between percentiles 70 and 100 constitute the last bin, the maximum surface variability.

### 3. Methodology

[12] The basic approach taken here is to compute the mean radiance for all defined solid angle intervals for a given surface type and topographical category and use the angular variability in the mean radiances to define the anisotropy. Ideally, the anisotropy should be determined at a very high angular resolution for each region and vegetation type. However, the limited sampling constraints necessitate compromises in angular resolution and surface type classification.

[13] To obtain statistically significant results, the data were binned and averaged in angular bins as functions of cloud fraction, surface type, and topography or terrain variability. Assuming azimuthal symmetry, the RAA span

**Table 1.** Surface Vegetation Type and Mean Surface Height Variability

	Vegetation Type	SV, m		
		Minimum	Medium	Maximum
IGBP number				
5 (1–5)	forest	0–7.6	7.6–34.5	>34.5
6	closed shrublands	0–13.3	13.3–33.2	>33.2
7	open shrublands	0–8.4	8.4–35.8	>35.8
8	woody savanna	0–9.6	9.6–21.4	>21.4
9	savanna	0–7.0	7.0–16.7	>16.7
10	grassland	0–14.0	14.0–68.2	>68.2
12	croplands	0–8.5	8.5–28.9	>28.9
14	crop mosaic	0–11.2	11.2–33.1	>33.1
16	barren desert	0–6.0	6.0–16.0	>16.0
Surface type				
I	10, 7	0–9.6	9.6–47.5	>47.5
II	5, 6, 8, 9, 12, 14	0–8.7	8.7–26.0	>26.0
III	16	0–6.0	6.0–16	>16.0

of  $0^\circ$ – $180^\circ$  was divided into nine bins of  $\Delta\phi_i = 20^\circ$  and the VZA range of  $0^\circ$ – $70^\circ$  was divided into seven  $10^\circ$  bins denoted by  $\Delta\theta_i$ . To account for illumination variations, three intervals of SZA are considered: (1)  $0^\circ$ – $48^\circ$ , (2)  $48^\circ$ – $70.1^\circ$ , and (3)  $70.1^\circ$ – $90^\circ$ . These ranges,  $\Delta\mu_o$ , correspond to equal spans of 0.33 in  $\mu_o$ , the cosine of SZA. Time-of-day segments rather than SZA bins were also considered for partitioning the data [Gambheer et al., 2002], but SZA was found to be a more robust independent parameter. Four cloud bins  $\Delta Ac$  are defined based on cloud amount: (1) clear ( $Ac \leq 5\%$ ), (2) partly cloudy ( $5 < Ac \leq 50\%$ ), (3) mostly cloudy ( $50 < Ac \leq 95\%$ ), and (4) overcast ( $Ac > 95\%$ ).

[14] A total of 9 vegetation types VT was used initially to gain insight into the dependence of anisotropy on the surface classification. The major vegetation types were taken from the original International Geosphere Biosphere Program (IGBP) scene types [Belward and Loveland, 1996]. No water, tundra, ice, snow, wetlands, or urban surfaces were considered. First, all IGBP forest types were combined into one forest class. Data from regions within the forest, savanna, woody savanna, grassland, open and closed shrublands, croplands, cropland-forest mosaics, and barren desert were then analyzed to determine how the azimuthal anisotropy varied for each classification. Table 1 lists the values of SV for each of the IGBP surface types. In general, the deserts and savannas are the flattest surface types while grass and open shrubs are most common on rough terrain.

[15] Bin averages of LW and WN radiance were computed for each individual vegetation type. The mean LW radiance for each category is

$$L_{LW}(VT, SV, Ac; \Delta\mu_o, \Delta\theta, \Delta\phi) = \frac{\sum L_{lw}(VT, SV, Ac; \Delta\mu_o, \Delta\theta, \Delta\phi)}{N(VT, SV, Ac; \Delta\mu_o, \Delta\theta, \Delta\phi)}, \quad (1)$$

where  $N$  is the number of samples from the total RAPS data set that meet the criteria for each category and  $L_{lw}$  is a single measurement. The summation is over  $N$  radiances. The mean WN radiance  $L_{WN}$  is also computed for each bin in the same manner as equation (1) from the WN measurements. The WN mean equivalent blackbody temperatures  $T_{WN}$  were computed from the bin averages of  $L_{WN}$  using the

Planck function at a wavelength of  $10 \mu\text{m}$ . Averages of  $\mu_o$ , VZA, and RAA were computed for every angular bin using all combinations of  $Ac$ , VT, and SV. For simplicity, it is assumed that all parameters are derived separately for different VT, SV, and  $Ac$  bins and these terms, shown before the semicolons in the arguments for each variable in equation (1), will not be shown explicitly hereafter.

[16] After averaging all data into the appropriate bins, the mean radiance  $L_{LWV}$  is computed for each VZA bin by averaging over RAA;

$$L_{LWV} = L_{LW}(\Delta\mu_o, \Delta\theta) = \frac{\sum_{i=1}^9 L_{LW}(\Delta\mu_o, \Delta\theta, \Delta\phi_i)}{9}. \quad (2)$$

These averages, which characterize the limb darkening for each case, are used to calculate the equivalent partial Lambertian radiance  $L_{LW_e}(\Delta\mu_o)$  by integrating  $L_{LWV}(\Delta\theta)$  over  $\theta = 0, 70^\circ$ . The relative limb darkening,

$$\gamma(\Delta\theta) = L_{LWV}(\Delta\theta)/L_{LW_e}, \quad (3)$$

is computed for each  $\Delta\theta$ . The magnitude of the VZA variation is given by  $L_{LWV}(\Delta\theta) - L_{LW_e}$ .

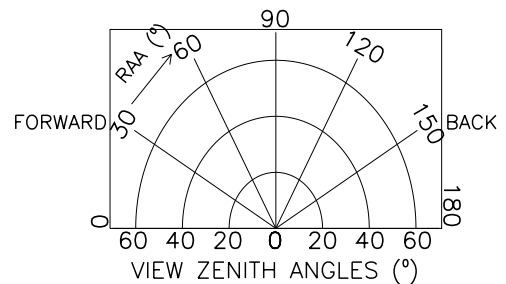
[17] To isolate the azimuthal anisotropy from limb darkening, the differences,

$$\Delta L_{LW}(\Delta\theta, \Delta\phi) = L_{LW}(\Delta\theta, \Delta\phi) - L_{LWV}(\Delta\theta), \quad (4)$$

are computed for each  $\Delta\mu_o$ . The resulting values are plotted following the convention shown in Figure 2. VZA varies along the x axis (radial axis) and RAAs are given along the polar direction with RAA =  $0^\circ$  at the extreme left. The RAA values between  $0^\circ$  and  $90^\circ$  correspond to forward scattering, when the satellite and Sun are on opposite sides of the zenith. RAAs between  $90^\circ$  and  $180^\circ$  correspond to the backscattering hemisphere with the satellite and Sun on the same side of the zenith. A normalized azimuthal correction factor,

$$\gamma_{LW}(\Delta\theta, \Delta\phi) = L_{LW}(\Delta\theta, \Delta\phi)/L_{LWV}(\Delta\theta), \quad (5)$$

is also computed to eliminate the sensitivity of the differences to the magnitude of the observed radiance and for use in correcting for the azimuthal effect. Similar quantities,  $\gamma_{WN}$ ,  $\Delta L_{WN}(\Delta\phi)$ ,  $L_{WNV}(\Delta\theta)$ , and  $L_{WNe}(\Delta\mu_o)$  were computed in the same manner for the WN radiances.

**Figure 2.** Plotting convention for radiance and temperature ( $T$ ) anisotropy.

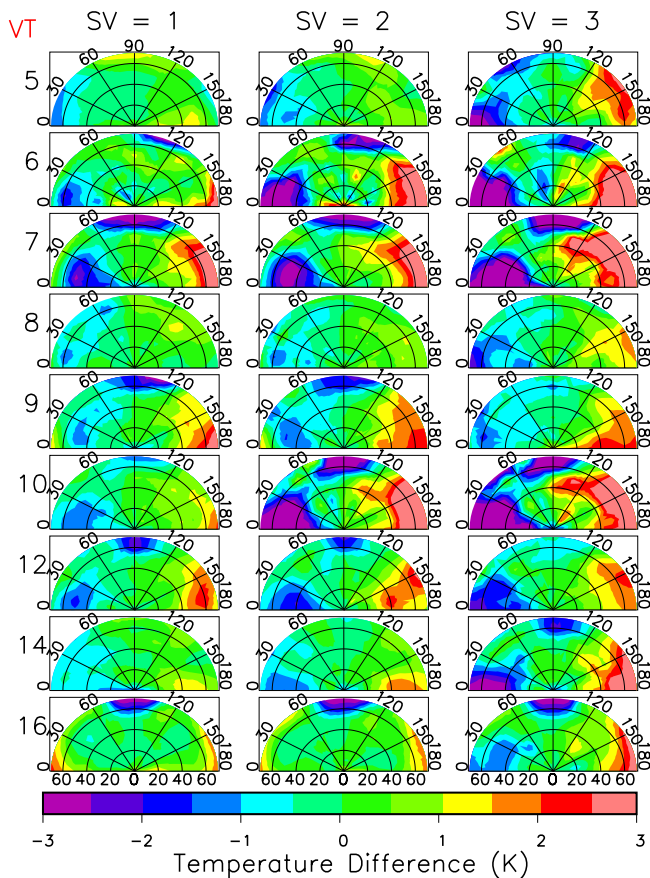


**Figure 3.** TRMM WN anisotropy  $\Delta T$  (K) for combined vegetation types for all surface variabilities for solar bin number 2.

$\Delta T(\Delta\theta, \Delta\phi)$  was computed by first converting  $L_{WN}(\Delta\theta, \Delta\phi)$  and  $L_{WNV}(\Delta\theta)$  to brightness temperatures  $T(\Delta\theta, \Delta\phi)$  and  $T(\Delta\theta)$ , respectively, using the 10- $\mu\text{m}$  Planck function and subtracting the latter from the former.

[18] The initial values of  $\Delta T(\Delta\theta, \Delta\phi)$  are plotted in Figure 3 for clear conditions over the original nine vegetation types for solar bin 2 ( $48.0^\circ \leq \text{SZA} < 70.1^\circ$ ). These plots demonstrate that the anisotropy varies substantially with VT and SV. The greatest ranges in  $\Delta T$  for each VT occur at the maximum surface variability. The minimum variability in  $\Delta T$  generally coincides with minimum SV. Overall, it appears that the maximum anisotropy occurs for regions covered with grass and open shrubs. The minimum anisotropy is apparent for woody savannas, croplands, and barren deserts. A few of the plots (e.g., for closed shrubs, VT = 6) in Figure 3 are relatively noisy. More noise occurs at other SZAs where the sampling is poorer.

[19] To minimize the noise, the vegetation types were combined to produce new surface types ST according to similarities in anisotropy. One objective measure of anisotropy is the difference between the mean temperatures  $T_i(\Delta\theta)$  in RAA bins  $i$  that mirror each other. This difference is

$$\Delta T_m = \Sigma\{(T_1 - T_9) + (T_2 - T_8) + (T_3 - T_7) + (T_4 - T_6)\}, \quad (6)$$

where the differences are computed for each VZA bin and summed over all VZA bins for the maximum SV category.

To achieve the maximum sampling, a total of 3 surface types were created by combining the IGBP VTs as indicated in the bottom portion of Table 1. The barren desert class had the lowest value of  $\Delta T_m$  and the greatest number of samples. Therefore it was not combined with any other VT and constitutes surface type 3. All further analysis only considers the anisotropy computed according to surface type instead of vegetation type with the parameter ST in place of VT in equation (1). Additionally, mean bin values were computed for every parameter including the SZA, RAA, and VZA.

## 4. Results

### 4.1. TRMM Clear Scenes

[20] Figure 4 shows an example of  $\gamma_{LW}(\Delta\theta)$  for clear conditions over all surface types and terrain variabilities. Surprisingly, limb darkening is consistently more pronounced for low SZAs (around noon) and is least for high SZAs. That is, the range in  $\gamma_{LW}(\Delta\theta)$  decreases with increasing SZA. This systematic limb-darkening behavior has not been previously observed and, because it is not taken into account in current limb-darkening corrections, could introduce a hitherto unknown source of uncertainty in the retrieval of LW flux from a radiance measurement. Based on the curves in Figure 4, the additional error could be as large as  $\pm 2\%$  in the instantaneous derived LW flux. Similar variations of  $\gamma_{LW}(\Delta\theta)$  with SZA were found for the WN data. Limb-darkening models were also derived from the nighttime CERES RAPS data. The results (not shown) fall in the middle of the curves in Figure 4 suggesting that heating and cooling of the surface during the day as well as other diurnally varying parameters such as humidity and boundary layer thermal structure alter the clear-sky limb-darkening characteristics.

[21] Figure 5 shows the corresponding values of  $\Delta L_{LW}$ , the deviation from simple limb darkening, for all three surface variabilities for SZA bin 2 over surface type. The patterns are similar to those in Figure 3, but are generally smoother. Negative values of  $\Delta L_{LW}$  predominantly occur on the shadowed side for all cases. Over deserts, the results are somewhat noisy for minimum and medium SV because the signal is small, except near VZA =  $70^\circ$ . For all SV and ST, the greatest positive values are found for VZA >  $40^\circ$  and for RAA >  $150^\circ$ . The minimum values tend to occur near VZA =  $50^\circ$ , RAA =  $0^\circ$  and around VZA =  $65^\circ$ , RAA =  $90^\circ$ . Higher resolution binning would provide more details of the anisotropy along the principal plane, but at the expense of reduced sampling. Differences as large as  $8 \text{ Wm}^{-2}\text{sr}^{-1}$  were found for ST = 1 and SV = 3 indicating that the anisotropy is very strong, even for average conditions. Radiance errors of that magnitude translate to flux errors of  $\sim 25 \text{ Wm}^{-2}$ . Greater or smaller differences will occur in any given instance. For each surface type, the contrast between forward and back scattering becomes more distinct as surface variability increases. The contrast enhancement is especially noticeable from the medium to maximum SV bins confirming that increased topographical shadowing enhances the temperature differences between illuminated and shadowed surfaces. Notably, for the grass and open shrub lands (ST = 1), the intense anisotropy is evident for all SV bins.

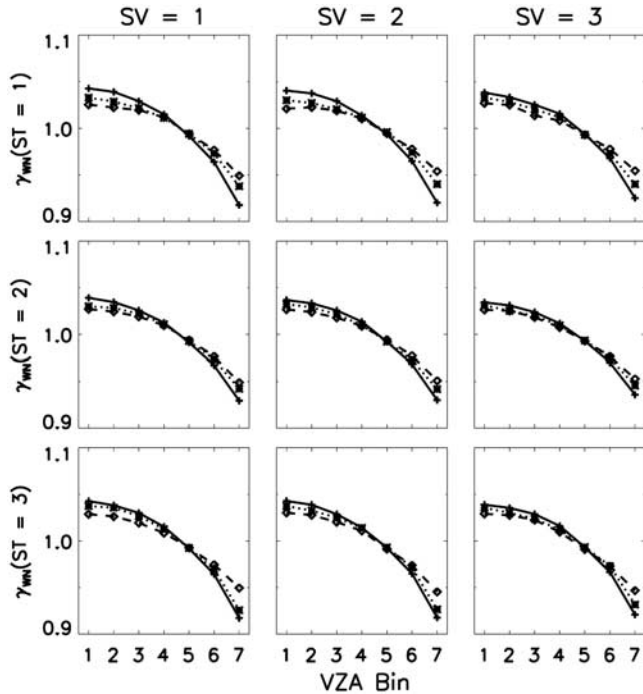


**Figure 4.** TRMM LW clear-sky limb-darkening functions from equation (3) for all surface types and variabilities. Solid line and pluses denote SZA bin 1; dotted line and asterisks denote SZA bin 2. Dashed line and diamonds indicate SZA bin 3.

[22] The WN anisotropy for all SZA bins is plotted in Figure 6 for  $ST = 1$  in terms of  $\Delta T$  over the full range of terrain variability. As expected, the patterns in  $\Delta T$  for SZA bin 2 are very similar to those for  $\Delta L_{LW}$  in the top row of Figure 5. Although not included in the color bar, mean temperature differences exceeding 8 K are observed between the sunlit and shaded sides. The patterns are similar for all times of day, but the maximum anisotropy occurs in the middle range of SZA. As SZA approaches  $0^\circ$ , the solar intensity maximizes as the relative area in shadow decreases. When the Sun is close to the horizon (SZA bin 3),

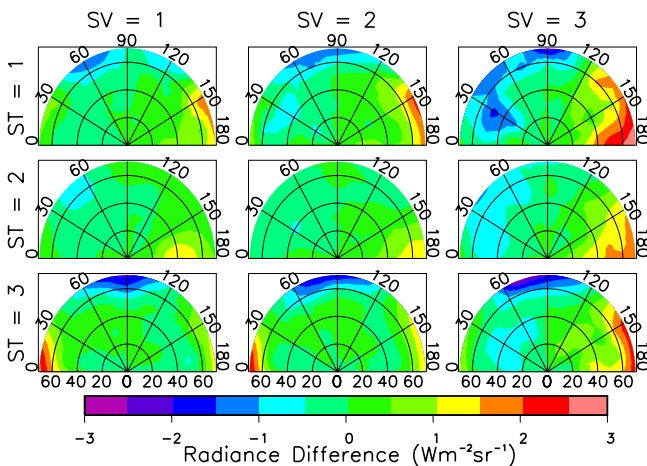


**Figure 5.** TRMM LW anisotropy  $\Delta L$  ( $W m^{-2} sr^{-1}$ ) for all surface types and variabilities for solar bin number 2.

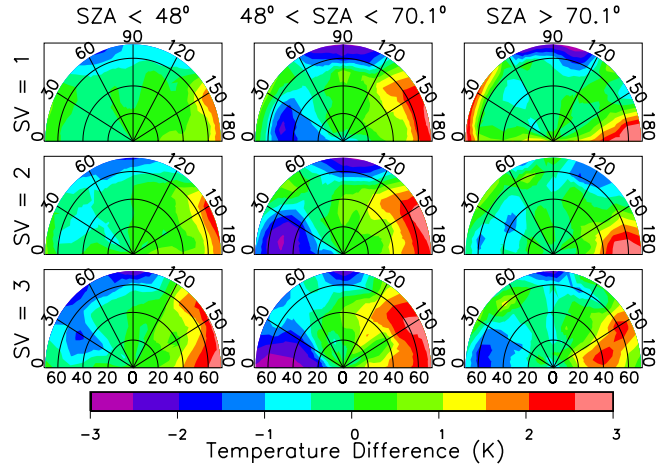


**Figure 6.** Solar zenith angle variation of TRMM WN anisotropy  $\Delta T$  (K) over surface type 1 for all surface variabilities.

the solar heating is relatively weak but the shadowing is at a maximum. Thus the anisotropy is not as strong as for SZA bin 2 and the maximum heating is confined to a smaller range of angles. However, a secondary maximum is evident for all SVs when  $VZA > 60^\circ$  and  $RAA < 60^\circ$  in this last SZA bin. Because of VZA limitations, it is not possible to determine if the anisotropy increases for  $VZA > 70^\circ$ . For the middle SZA bin, the minimum along  $RAA = 0^\circ$  tends to broaden with increasing surface roughness. The secondary minimum near  $RAA = 90^\circ$  and  $VZA = 60^\circ$  is generally broader for smoother surfaces.

[23] The variation of  $\Delta T$  with SZA for the other surface types is similar but less pronounced. In Figure 7, the secondary maximum in the forward direction is evident for SZA bin 3 for desert surfaces with maximum terrain variability. The largest positive values are all found at RAAs between  $120^\circ$  and  $180^\circ$ . Similar patterns are observed for other terrain conditions for  $ST = 2$  and 3 although the anisotropy is less pronounced. Similar analyses over ocean yield no distinct patterns with  $L_r$  varying by less than  $1.0 W m^{-2} sr^{-1}$  or 1.0 K. To understand the statistical significance of the anisotropy in Figures 6 and 7, standard errors in the bin means were computed as  $SE = SD (N - 1)^{-1/2}$ , where

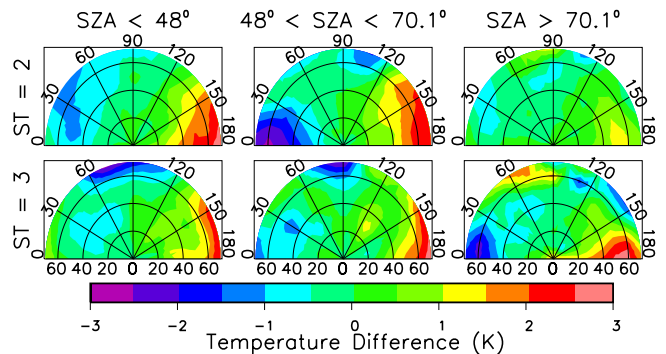


**Figure 7.** Solar zenith angle variation of TRMM WN anisotropy  $\Delta T$  (K) over surface types 2 and 3 for all maximum terrain variability (SV = 3).

SD is the bin standard deviation and  $N$  is the number of samples. The standard errors are found to be no greater than 5% of the means for all clear cases. Thus differences exceeding 0.3 to 0.6 K, depending on the bin and SV are significant at the 99% confidence level.

#### 4.2. TRMM Cloudy Scenes

[24] Clouds also cause shadowing and should introduce some anisotropy in the emerging infrared radiation field. Figure 8 shows the WN  $\Delta T$  over grass and open shrublands ( $ST = 1$ ) for cloudiness increasing from partly cloudy (PC) to overcast (OC) conditions. As in the clear case (Figure 6), the shadowed side is cooler than the sunlit side for the first solar bin (Figure 8a) for all terrain and cloud cover conditions. The anisotropy for the PC scenes is similar in magnitude to that seen for clear conditions while it is actually larger than the clear cases for the mostly cloudy (MC) and OC conditions. Maximum anisotropy occurs for the medium topography category. Overall, the contours are much noisier than those for the clear case. The noise increases with SZA. For SZA bin 2 (Figure 8b), there remains some substantial anisotropy for the PC conditions, but the shadow-sunlit contrast is somewhat diminished for the MC cases. The OC scenes yield no significant patterns at higher Sun angles. Significant anisotropy is also evident for PC and OC cases for SZA bin 3 (not shown), but not for overcast conditions. Overall, the strongest anisotropy was found for SZA bin 1. Similar results were found for surface type 2. The  $\Delta T$  patterns for desert clouds are much noisier, in general, presumably because of fewer cloud samples. The mean cloud cover is roughly 22, 74, and 98% for the PC, MC, and OC cases, respectively.

[25] It is not surprising that the shade-sunlit pattern of  $\Delta T$  observed for clear conditions is, to a great extent, replicated in the PC and MC scenes. When the satellite and Sun are coaligned, the satellite will measure radiation emanating from the clouds and only the illuminated areas on the surface. Conversely, when the satellite views in the forward direction, it presumably measures the same radiance field from the clouds, but now only measures the shadowed surface areas resulting in a lower overall radiance. The surface skin temperature responds almost immediately to changes in cloud cover [Duda and Minnis, 2000], so the shading effect is unlikely to be diminished very much in a long-term average by cloud movement that exposes a scene to alternating illumination and shading. The unexpected result in these data is the relatively strong signal for OC conditions in SZA bin 1. This effect is most likely due to inclusion of optically thick and thin clouds in the OC classification. The thin clouds will cause some shadowing but will also permit some of the WN radiation to pass through the cloud. At higher SZAs, the increased path length of the cloud eliminates the direct solar beam required for shadowing. Thus even if the same amount of optically thin clouds is present for both SZA bins 1 and 2, the amount of shadowing for the former will be considerably greater than that for SZA bin 2.

#### 4.3. Terra Anisotropy

[26] Figure 9 shows  $\Delta T$  for the grass and shrub lands ( $ST = 1$ ) for SZA bin 2 as derived from the Terra data. The basic patterns for the clear scenes are much the same as

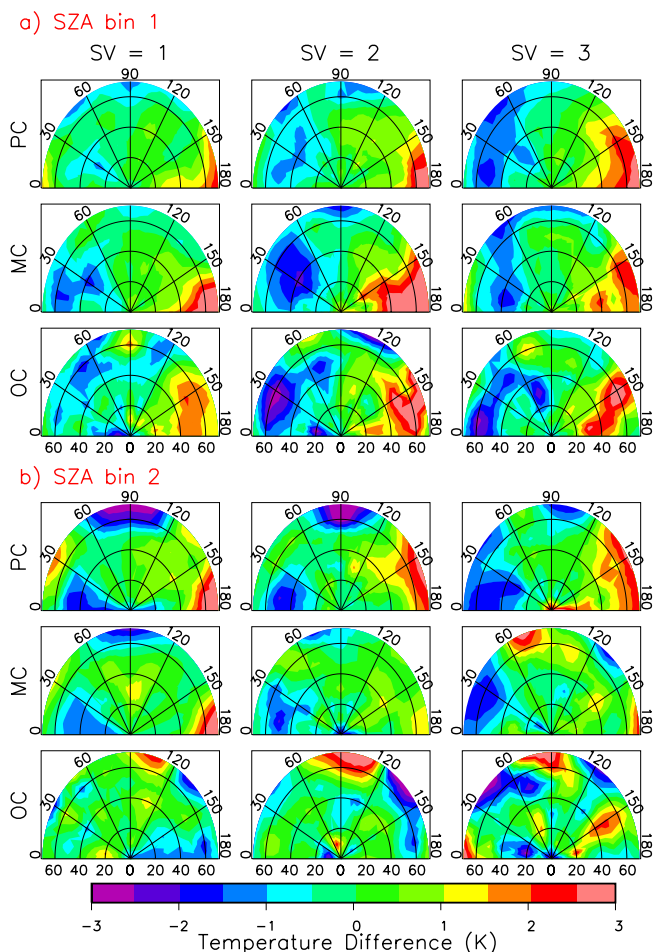


**Figure 8.** TRMM WN anisotropy for grass and open shrubs ( $ST = 1$ ) under different cloud conditions: partly cloudy (PC), mostly cloudy (MC), and overcast (OC).

those seen in Figure 6 from the TRMM data. However, the contours are smoother and the anisotropy is more pronounced. Nearly all positive values are confined to  $RAA > 90^\circ$  and the negative values to  $RAA < 90^\circ$ . No secondary minima occur around  $VZA > 50^\circ$ ,  $RAA = 90^\circ$  as seen in the middle column of Figure 6. The Terra clear-sky results for the other two surface types are very similar to those in Figure 9 with smoother contours and distinct positive-back and negative-forward differences. Compared to the results for  $ST = 1$ , the magnitude of the anisotropy is less for  $ST = 2$  and least for  $ST = 3$  as seen for the TRMM data in Figures 5 and 6. The sampling was insufficient to obtain representative results for the other two SZA bins.

[27] The dissipation of the anisotropy signal with increasing cloud cover is clearly evident in Figure 9. For all three SVs, the magnitudes of the minimum and the maximum  $\Delta T$  both decrease with cloud amount. For overcast scenes, the distinct shading-illumination pattern is no longer evident. The contours for the cloudy cases in Figure 9 are much smoother than their counterparts in Figure 8b suggesting that the anisotropy for nonovercast scenes is well behaved. Similar results were found for the cloudy classes in SZA bin 2 for desert and forest surfaces. Initial analyses using the

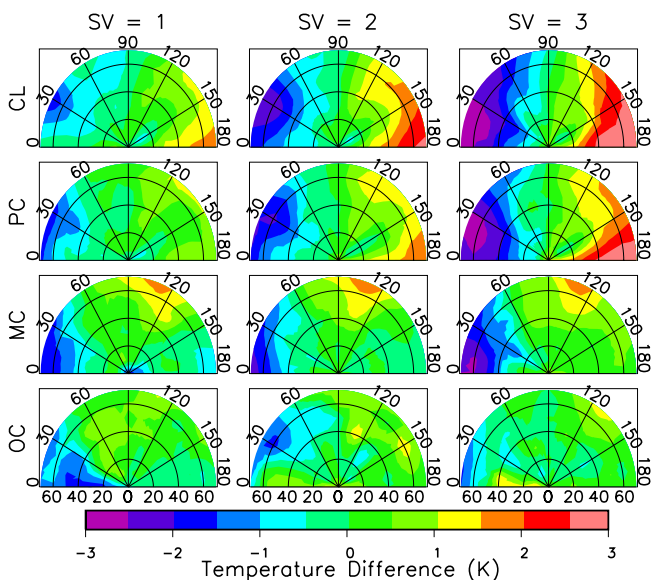


**Figure 9.** Terra WN anisotropy  $\Delta T$  (K) for SZA bin 2 for surface type 1. CL denotes clear scenes.

Aqua CERES data for January 2003 yield results that are very similar to those in Figure 9 indicating that the SZA dependence of anisotropy is independent of time of day. Likewise, computation of  $\Delta T$  for Terra data separately from each of the 3 years yields nearly identical contours indicating that the results in Figure 9 are stable and representative of any year.

## 5. Discussion

[28] The results confirm that thermal infrared radiances are predictably greater when viewing the sunlit side of a land scene and smaller for shadowed conditions. Thus the results should be valuable for correcting for the anisotropy. Before exploring correction techniques, it is necessary to understand the peculiarities of the data sets and the potential uncertainties.

### 5.1. Surface and Terrain Dependence

[29] Azimuthal dependence of radiance appears to be a stronger function of topographical variability than vegetation type. The RAA variation is largest for shrublands and grasslands and least for deserts. Over deserts, it is less consistent than over other types possibly as a result of dramatic variability in surface albedo between regions. Such variability may not be sampled at all angles and could introduce some biases and perhaps reduce the overall anisotropy. The shrublands and grasslands probably produce more anisotropy in flatter terrain because there is more space between the vegetation than in forests. Shadows cast by trees in continuous forests are often not observable because adjacent trees block the view of the surface. Over barren deserts, only rocks are available to cast shadows in flat lands. Terrain and vegetation still have impacts in partly and mostly cloudy conditions but the clouds are the primary shadow makers. Therefore surface effects are somewhat muted. The results represent average terrain conditions. Therefore greater anisotropy is likely to

occur in very rugged terrain as found by *Minnis and Khaiyer* [2000].

### 5.2. Sampling

[30] Both satellite data sets yield similar, but not identical results. Most of the TRMM  $\Delta T$  patterns in Figures 6 and 7 have a relative maximum in the forward direction that separates the minima at RAA = 0° and 90° and that is not seen in the Terra results. These differences could be due to different sampling patterns or to discrepancies in the scenes and months that were sampled. To examine the latter, the anisotropy was computed by constraining the Terra data to the period January through August and to land between 33°S and 33°N to match the territory observed by TRMM. No significant differences were found using either the original or constrained Terra data indicating that the TRMM-Terra differences are not due to differences in geographical or seasonal sampling.

[31] The TRMM and Terra temporal and angular sampling patterns, however, are dramatically different. TRMM might sample a given region once or twice per month in a given SZA bin while Terra samples a given region nearly every day, mostly in the same SZA bin. The frequency of viewing a particular set of angles also differs because of the different orientations of the satellite relative to the solar plane and the constraints in the angular coverage of TRMM due to the VIRS VZA limit of 48°. Figure 10 shows examples of TRMM and Terra sampling for SZA bin 2 over surface type 1 in clear skies. Maximum sampling occurs around VZA = 50° for TRMM while the Terra sampling peaks near VZA = 70° in the backscattering direction. Sampling is least for TRMM around VZA = 70°, RAA = 90°. This is significant in that the secondary minimum also occurs at this angular bin (Figure 6). The Terra minimum is generally between VZAs of 10 and 50° at low values of RAA. These sampling patterns are fairly typical for most of the surface types and SZA bins. The number of samples per day is smaller for the Terra data set, but overall, the total number of samples is greater for Terra

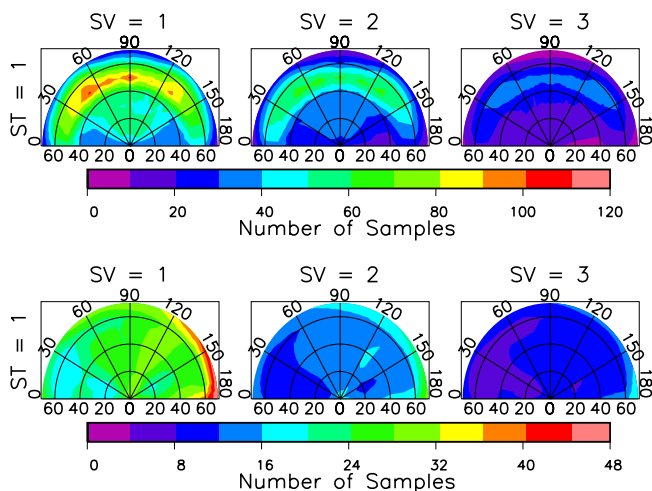


**Figure 10.** Angular distribution of mean number of daily samples for TRMM (68 days) and Terra (753 days) for SZA bin 2 for clear scenes.

since TRMM only provided 68 days of data compared to 753 for Terra.

[32] Another distinct difference is the orientation of Sun-synchronous satellites like Terra. Because its path is nearly in a north-south orientation and it crosses the equator at the same time of day, the scans to the east of the satellite are always observing areas at an earlier local time than those to the west of the satellite. The MODIS swath width of 2300 km translates to approximately 1.7 and 2.9 hours at latitudes of  $33^\circ$  and  $60^\circ$ , respectively. Thus the land at the eastern end of the swath will be viewed at a local time that is 1.5–3 hours later than that at the western end of the swath. For a morning orbit, the eastern land view should, on average, yield warmer brightness temperatures even without any azimuthal anisotropy, because the observed surface has been heated by the Sun longer than the land to the west. In the construction of plots like those in Figure 9, it is generally assumed that such time differences will be averaged out because a given location will be viewed from both directions over time. But this may not necessarily be true for Sun-synchronous satellites because time of day is linked to RAA. Views to the east between  $60^\circ\text{N}$  and  $60^\circ\text{S}$  are nearly always in the forward hemisphere and, conversely, the western views are in the back scattering hemisphere. Thus, in clear conditions, the mean temperature of the forward hemisphere should be greater than its converse because of the local time difference, an effect that would tend to diminish shadow-induced anisotropy. The TRMM orbit also has some time-space sampling biases, but these are more difficult to explain because the variable Earth-Sun geometry is considerably more complex than that for the Sun-synchronous satellites.

[33] Examples of the TRMM mean Sun angles for clear scenes over ST = 2 in Figure 11a indicate  $\mu_o$  ranges from 0.78–0.87, 0.50–0.56, and 0.10–0.22 for SZA bins 1, 2, and 3, respectively. For the last two SZA bins, the maximum values tend to occur at high values of VZA while the minima are near nadir. The opposite occurs for the first SZA bin. For SZA bin 2, the maximum  $\mu_o$  occurs near the minimum in sampling (Figure 10a) and the secondary minimum in  $\Delta T$ .

[34] By binning the data into SZA bins, it is assumed that for Terra, the time-space-angle biases discussed above can be minimized. For SZA bin 2, this is possible because the eastern scans at high latitudes will provide samples at the upper end of the SZA range. Conversely, western views at lower latitudes will produce samples for the lower end of the range. That kind of tradeoff is not possible for the other two SZA bins. Figure 11b shows the mean values of  $\mu_o$  for the Terra data corresponding to the TRMM data in Figure 11a. No sampling was available in SZA bin 3 because of the latitudinal restrictions. The east-west bias is clearly evident for SZA bin 1 where no compensation can occur. The east-west effect is noticeable for SV = 1 in SZA bin 2, but is not evident for the other terrain categories.

[35] Although it remains difficult to quantify, it is clear that the Terra data provide smoother patterns for SZA bin 2 because of more uniform angular-bin sampling, greater numbers of samples overall, and more homogeneous sampling of the SZA range. Thus it is concluded that for SZA bin 2, the Terra results are probably more represen-

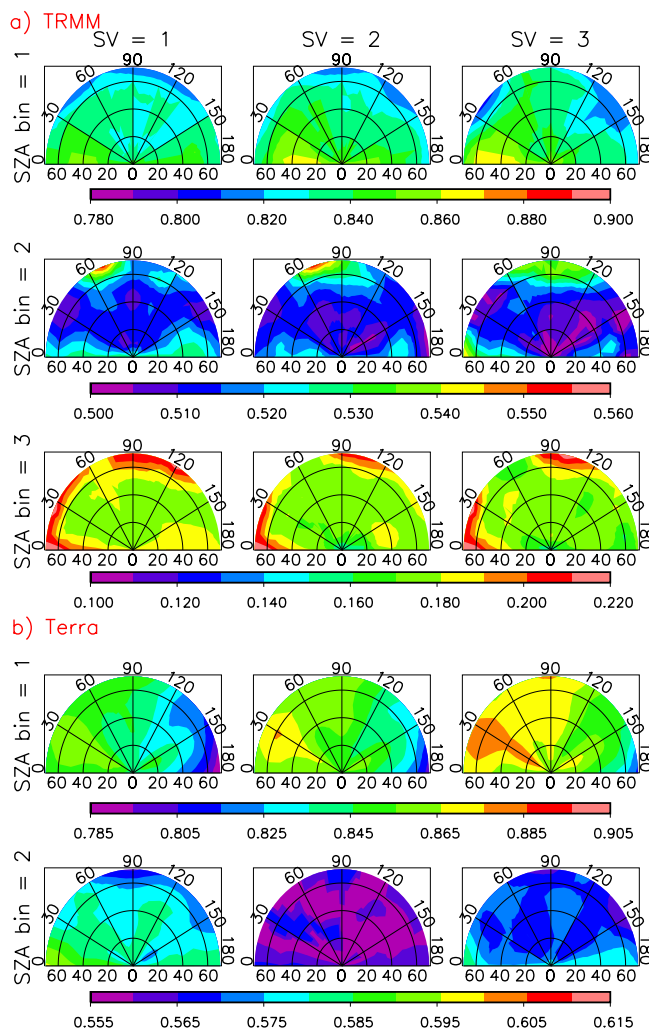


**Figure 11.** Angular distribution of mean  $\cos(\text{SZA})$  for clear skies over surface type 1 from (a) TRMM and (b) Terra data.

tative of the LW and WN anisotropy. However, because TRMM data provide reasonable sampling over all solar angles and surfaces and are similar to the bin-2 Terra results, the TRMM data, overall, provide a better characterization of the anisotropy that could be used to correct measurements of radiances in the thermal infrared spectrum. The TRMM data alone also provide sampling over all SZA bins for the same regions. Although combining the TRMM and Terra data sets would offer improved sampling (more uniform bin coverage) and less noise overall, it would be necessary to increase the latitudinal coverage and thereby change the regional coverage as a function of SZA. It is beyond the scope of this study to consider that combination and analyze the possible latitudinal biasing of the SZA dependence that accompanies the use of the Terra data. Such analyses are deferred to future study.

### 5.3. Clear-Sky Model and Validation

[36] A simple bidirectional emission model (BDEM) was developed to account for LW and WN azimuthal anisotropy in clear conditions based on the CERES TRMM bin-

averaged radiances reported above. The model computes the LW or WN anisotropic factor,

$$R(\text{ST}; \text{SV}, \mu_o, \text{VZA}, \text{RAA}) = \pi L' / M', \quad (7)$$

where  $L'$  and  $M'$  are linearly interpolated radiance and flux, respectively.  $L'(\text{ST}; \text{SV}, \mu_o, \text{VZA}, \text{RAA})$  is obtained by sequentially interpolating between the bin mean radiances with respect to VZA, RAA,  $\mu_o$ , and SV for a particular surface type. The bin mean fluxes,  $M(\text{ST}, \text{SV}; \Delta\mu_o)$ , were computed by integrating the bin-averaged radiances over all RAA and VZA. Since the number of pixels sampled by TRMM is inconsequential beyond  $70^\circ$ , it was necessary to estimate radiance values for the last two VZA bins ( $70^\circ$ – $80^\circ$  and  $80^\circ$ – $90^\circ$ ). The missing radiance values were estimated using a quadratic fit to the radiances from the filled VZA bins in a given RAA bin.  $M'(\text{ST}; \text{SV}, \mu_o)$  is obtained by interpolating between the bin mean fluxes in the same manner used for radiance, except that there is no interpolation with respect to VZA and RAA. In the radiance or flux interpolation sequence, linear extrapolation is used whenever the value of a given input parameter such as SV is less than or greater than the mean value of the same parameter in the first or last bin, respectively. The bin means are assumed to be representative values at the centers of each bin.

[37] To test the WN BDEM, the GGEO data were adjusted to the VZA and RAA of temporally and spatially matched SFC VIRS radiances. The spatial matching was automatic because of the  $1^\circ$  gridding. To maximize the number of samples and minimize temporal changes, only GGEO data taken within 15 min of the SFC data were used. Mean values of SV were computed for each  $1^\circ$  region. If the region contains more than one scene type, the one covering the greatest portion of the region was used to select ST. The model was used to compute  $R_1$  and  $R_2$ , the WN anisotropic factors, where the subscripts 1 and 2 refer to GGEO and SFC, respectively. The BDEM performance can be evaluated using the difference  $\Delta T$  between the observed GGEO temperature and the GGEO temperature adjusted to the SFC viewing perspective:

$$\Delta T = B^{-1}\{L_1\} - B^{-1}\{L_2(R_1/R_2)\}, \quad (8)$$

where  $L_1$  and  $L_2$  are the SFC and GGEO radiances, respectively and  $B^{-1}$  is the inverse Planck function for the VIRS  $10.8\text{-}\mu\text{m}$  channel. If the satellite imagers are accurately intercalibrated and the BDEM is perfect,  $\Delta T = 0$ .

[38] To ensure that the satellite imagers are properly intercalibrated, the matched data were screened to obtain a subset containing mean radiance pairs with nearly the same values of RAA and VZA. Temperature differences were computed for mean radiance pairs having differences in VZA and RAA that are less  $5^\circ$  and  $5^\circ$ , respectively. The results summarized in Table 2, show that overall, the VIRS temperatures are roughly  $0.6 \pm 0.1$  K less than their GGEO counterparts. The differences are nearly the same for all three satellites. Similar results were found using the looser angular restrictions of Minnis *et al.* [2002b]. Thus, if the models produce accurate corrections, the mean value of  $\Delta T$  should be about  $-0.6$  K.

**Table 2.** Differences Between Matched SFC VIRS and GGEO  $1^\circ$   $11\text{-}\mu\text{m}$  Brightness Temperatures for Temporally Matched Data Taken With Differences in VZA and RAA Less Than  $5^\circ$  and  $5^\circ$ , Respectively

Satellite	Mean, K	RMS, K	Number of Samples
GOES-8	-0.51	0.63	14
Meteosat-6	-0.64	1.49	54
GMS-5	-0.61	0.85	16
All	-0.61	1.28	84

[39] The remaining matched pairs of GGEO and SFC data were screened to remove navigationally mismatched data and mean radiances corresponding to the VIRS channel saturation temperature of 324 K, a potential source of bias. The resulting values of  $\Delta T$  from the filtered data were then used to compute the mean bias and root-mean square (RMS) difference for each scene type and all nine azimuthal bins. To determine if the azimuthally dependent model represents an improvement over a limb-darkening-only method, the GGEO results were also adjusted to the SFC view using the LDM,  $\gamma(\text{ST}; \text{SV}, \mu_o, \Delta\theta)$ , from equation (3). Table 3 lists the RMS and bias differences as a function of the VIRS RAA for all matched data excluding those used for the coangled comparisons in Table 2. The LDM bias errors are positive in the first seven azimuth bins while all but two of the BDEM bias errors are small negative values. Although the GGEO data are probably taken at many different RAAs for a given SFC azimuth bin, the data plotted in Figures 5 and 6 indicate that the minimum and maximum radiances should occur in the forward and back scattering directions, respectively. The LDM bias errors are consistent with this RAA behavior. On the other hand, the BDEM bias errors show no systematic variation with  $\Delta\phi$  and reduce the mean bias to roughly  $-0.5$  K indicating that the model is working in proper direction. Additionally, the BDEM RMS errors are reduced by 30–42% less than their LDM counterparts. The largest errors occur for RAA bin 4 where the differences between the TRMM and Terra results are greatest. This result suggests that some improvement might be gained by using the Terra data where they are applicable.

[40] Table 4 summarizes the differences as a function of the surface variability. For the flat surfaces ( $\text{SV} = 1$ ), the LDM and BDEM biases are nearly the same. However, the BDEM reduces the RMS error by 28% even for surfaces with little topography. The LDM bias increases to 0.6 K in the medium topography class and up to 2.6 K for  $\text{SV} = 3$ . That bias is 3.4 times greater than its BDEM counterpart. Nevertheless, not all of the bias was removed by the BDEM for  $\text{SV} = 3$ . Notably, the BDEM RMS errors are 45 and 51% less than the corresponding LDM values for  $\text{SV} = 2$  and 3, respectively. As expected, the greatest impact is realized for the roughest terrain. Overall, the BDEM bias error is 0.5 K closer than the LDM bias to the mean difference for the coangled data in Table 2 indicating that, on average, this simple model can be used to account for the anisotropy of infrared radiation for clear land surfaces during daytime. The RMS error is reduced by 38% relative to the LDM. It is 0.5 K greater than the RMS difference for the coangled data compared to 1.6 K for the LDM. Figure 12 shows scatterplots of the GGEO and VIRS data before and after applying the BDEM correction. The LDM correction actually resulted

**Table 3.** Difference Between GGEO 11- $\mu\text{m}$  Brightness Temperatures and SFC Temperatures Corrected to GGEO Angles Using Limb-Darkening Models (LDM) and Bidirectional Emission Models (BDEM)

SFC VIRS Azimuth Bin	LDM Bias, K	LDM RMS, K	BDEM Bias, K	BDEM RMS, K	Samples
1 (0–20°)	0.66	2.91	–0.10	1.86	358
2 (20–40°)	0.12	2.63	–0.40	1.67	436
3 (40–60°)	0.25	2.36	–0.34	1.66	646
4 (60–80°)	0.82	3.20	–0.08	2.01	903
5 (80–100°)	0.26	2.95	–0.21	1.71	1158
6 (100–120°)	0.96	2.96	0.41	1.73	835
7 (120–140°)	0.44	2.89	0.06	1.70	639
8 (140–160°)	–0.12	2.85	–0.16	1.77	644
9 (160–180°)	–0.11	2.73	–0.04	1.73	576

in a larger RMS error than that for the raw data plotted in Figure 12a. The BDEM correction (Figure 12b) noticeably reduces the scatter and decreases the RMS difference by 0.5 K relative to the uncorrected data in Figure 12a. These results indicate that the azimuthal anisotropy is the dominant error source since the LDMs worsened the comparisons.

[41] As seen earlier, the TRMM WN patterns are probably not the most accurate representation of the anisotropy because of sampling biases. Furthermore, the WN spectrum includes ozone and water vapor absorption lines not found in most of the GGEO and VIRS absorption bands. The stronger limb darkening by these absorbers may be responsible for some of the increase in RMS error resulting from the application of the LDMs to the IR data discussed earlier. Despite the inaccuracies and spectral discrepancies, the crude model developed here from the TRMM data significantly improves the estimation of IR temperatures at different angles compared to LDMs. This improvement is realized even though the VIRS scan patterns and latitudinal limitations probably minimized the impact of the maximum anisotropy because it typically occurs at  $VZA > 50^\circ$ . All of the VIRS and most of the GGEO data were taken at  $VZA < 50^\circ$ . Thus even greater error reductions are possible even with this early model.

[42] The LDMs used here are not the same as those developed by *Loeb et al.* [2003]. However, the error reductions would probably be similar because the *Loeb et al.* [2003] models are based on the WN channel and do not account for the azimuthal effects. The current LDMs are based on the same data set used by *Loeb et al.* [2003] but are formulated differently. The latter are parameterized based on the surface type, total column precipitable water, and the lapse rate between the skin temperature and the air temperature at a pressure level 300-hPa lower than that at the surface. It is not clear that that particular formulation would account for the SZA dependence seen in Figure 4. Further study is needed to examine the source of the SZA dependency of limb darkening and whether the lapse rate formulation would account for it. Ideally, the azimuthal anisotropy observed here and the SZA dependence of limb darkening could be included in later versions of the LW and WN models as developed by *Loeb et al.* [2003].

#### 5.4. Correlations With Shortwave Anisotropy

[43] Another approach for developing analytical BDEMs could make use of relationships between SW bidirectional

reflectance models and the LW anisotropy. *Minnis and Khaiyer* [2000] found that the difference in brightness temperature between two satellites is highly correlated with the difference in the normalized bidirectional reflectance distribution functions (BRDF) for clear landform *Minnis and Harrison* [1984]. The slope of the linear correlation was found to be proportional to the terrain variability. Although a complete examination of the relationship between SW and LW anisotropy is beyond the scope of this paper, an initial analysis of the data is warranted to determine if the SW-LW connection might serve as a potential means for developing an analytical model from the CERES data. The BRDFs from *Loeb et al.* [2003] were used to calculate the BRDF correction factor  $\chi(\text{SZA}, \text{VZA}, \text{RAA})$  for each of the angular bins for the clear categories for all SZA and ST classes. The mean factor  $\chi_v(\text{SZA}, \text{VZA})$  was also computed by averaging over all RAA bins at a given VZA. The BRDF difference factor

$$\Delta\chi(\text{SZA}, \text{VZA}, \text{RAA}) = \chi(\text{SZA}, \text{VZA}, \text{RAA}) - \chi_v(\text{SZA}, \text{VZA}), \quad (9)$$

was also computed for each angular bin to isolate the azimuthal SW effect. Figure 13 shows a scatterplot of  $\Delta\chi$  and  $\Delta T$  for all of the angular bins at  $\text{SZA} = 60^\circ$  for  $\text{SV} = 3$  and dark lands as defined by *Loeb et al.* [2003]. Overall, the squared linear correlation coefficient is 0.81 even without accounting specifically for differences in SV. This level of correlation indicates that the SW-LW anisotropy relationship is a strong candidate for developing advanced models to correct for LW azimuthal anisotropy.

## 6. Concluding Remarks

[44] It is clear from all of the results that more thermal radiation is observed on the sunlit side than on the shadowed side in most atmospheric conditions over land. Although no ideal data sets exist yet to perfectly measure the behavior of this anisotropy over all solar zenith angles, the CERES TRMM RAPS data provide sufficient information to reduce multiangle IR temperature prediction errors by 35% or more over the full range of daylight conditions. More sophisticated anisotropic correction formulations including TRMM, Terra and Aqua data could yield more accurate representations and further reduce the errors. Such models could be more analytical and might include information from bidirectional reflectance models to account for the shadowing of particular surface types. The azimuthal anisotropy is also significant in scenes containing clouds. Future model formulations should take this effect into account, perhaps in the form of additional parameters such

**Table 4.** Same as Table 3, Except as Function of Surface Variability

SV Class	LDM Bias, K	LDM RMS, K	BDEM Bias, K	BDEM RMS, K	Samples
1	–0.14	2.47	–0.19	1.78	3451
2	0.63	2.88	–0.13	1.59	2131
3	2.57	4.49	0.75	2.22	613
All	0.39	2.87	–0.08	1.77	6195

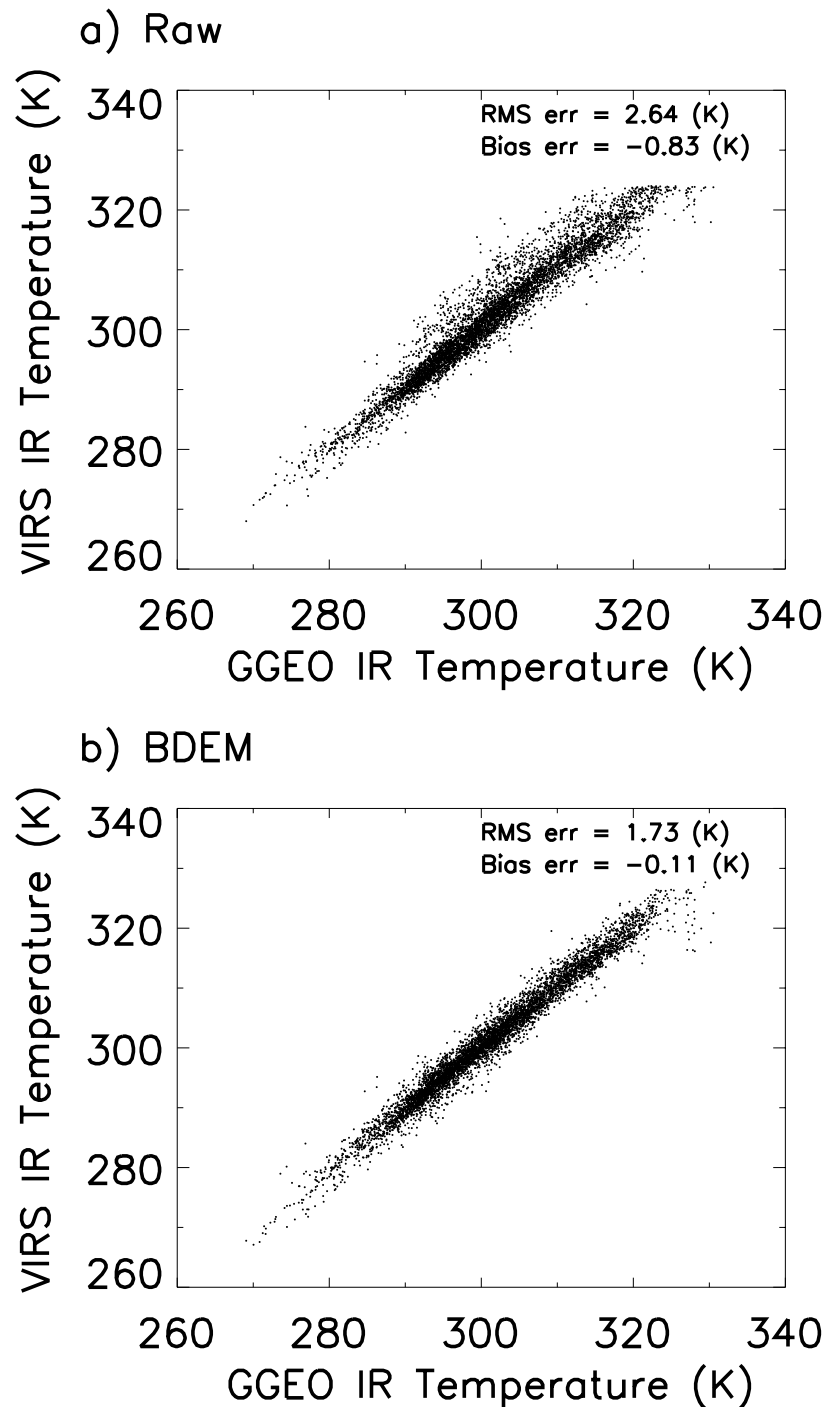


**Figure 12.** Scatterplots for matched data set (between GGeo and VIRS) WN temperatures with (a) no corrections and (b) BDEM corrections. RMS and bias errors are indicated for the 6195 matched  $1^\circ$  boxes. GGeo includes Meteosat-6, GMS, and GOES-8 data.

as cloud amount, phase, temperature, and optical depth. This study did not examine the anisotropy dependence on horizontal resolution. Such a dependency should be considered in future analyses.

[45] Infrared anisotropy over land is clearly a source of error that can be minimized with the available CERES data sets. The current formulation of the bidirectional emission model can be used to reduce LW flux errors for clear scenes and to improve skin temperature retrievals. The reductions

in skin temperature retrieval errors could be evaluated using data from surface radiometer sites and retrievals from geostationary satellite data. Additional testing of the current model should be pursued using matched Terra and TRMM WN and LW data because they are spectrally consistent with the model data. Both radiance and flux errors could be assessed. Implementation of the model should yield smaller instantaneous errors in LW fluxes from CERES and reduce biases in the LW radiation field measured by the Geosta-

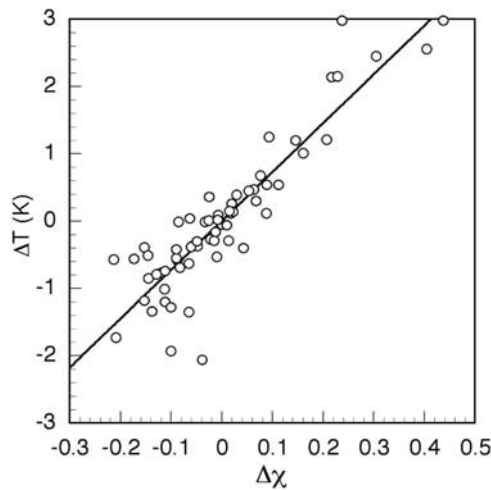


**Figure 13.** Scatterplot and linear regression fit for mean WN azimuthal temperature differences and SW BRDF difference factor for average clear scenes over dark land surfaces and SV = 3 at SZA = 60°.

tionary Earth Radiation Budget instrument on Meteosat-8. Additionally, more accurate instantaneous estimates of surface skin temperature from IR imagers on all geostationary satellites should be possible with these proposed corrections.

[46] **Acknowledgments.** Thanks to Mandy Khaiyer for help in the preparation of the figures and to Sandy Nolan and Nitchie Manalo-Smith for help with the CERES SSF data and to Norman Loeb for his helpful advice. This research was supported by the NASA Earth Science Enterprise Radiation Science Program through the CERES Project.

## References

- Belward, A., and T. Loveland (1996), The DIS 1-km land cover data set: Global change, *IGBP Newslett.*, 27, 7–9.
- Coulson, K. L., G. M. Bouricius, and E. L. Gray (1965), Optical reflection properties of natural surfaces, *J. Geophys. Res.*, 70, 4601–4611.
- Duda, D. P., and P. Minnis (2000), A study of skin temperature/cloud shadowing relationships at the ARM SGP site, paper presented at 10th ARM Science Team Meeting, Atmos. Radiat. Meas. Program, San Antonio, Tex., 13–17 March. (available as [http://www.arm.gov/docs/documents/technical/conf\\_0003/duda-dp.pdf](http://www.arm.gov/docs/documents/technical/conf_0003/duda-dp.pdf))
- Gambheer, A. V., D. R. Doelling, and P. Minnis (2002), Examination of the azimuthal variation of longwave radiance from CERES data, in *Proceedings of the 11th AMS Conference on Atmospheric Radiation*, pp. 160–163, Am. Meteorol. Soc., Boston, Mass.
- Garand, L. (2003), Toward an integrated land-ocean surface skin temperature analysis from the variational assimilation of infrared radiances, *J. Appl. Meteorol.*, 42, 570–583.
- Kimes, D. S., and J. A. Kirchner (1983), Directional radiometric measurements of row-crops temperatures, *Int. J. Remote Sens.*, 4, 299–311.
- Loeb, N. G., N. Manalo-Smith, S. Kato, W. F. Miller, S. Gupta, P. Minnis, and B. A. Wielicki (2003), Angular distribution models for top-of-atmosphere radiative flux estimation from the Clouds and the Earth's Radiant Energy System instrument on the Tropical Rainfall Measuring Mission satellite. Part I: Methodology, *J. Appl. Meteorol.*, 42, 240–265.
- Minnis, P., and E. F. Harrison (1984), Diurnal variability of regional cloud and clear-sky radiative parameters derived from GOES data, part III: November 1978 radiative parameters, *J. Clim. Appl. Meteorol.*, 23, 1032–1052.
- Minnis, P., and M. M. Khaiyer (2000), Anisotropy of land surface skin temperature derived from satellite data, *J. Appl. Meteorol.*, 39, 1117–1129.
- Minnis, P., D. F. Young, B. A. Wielicki, D. P. Kratz, P. W. Heck, S. Sun-Mack, Q. Z. Trepte, Y. Chen, S. L. Gibson, and R. R. Brown (2002a), Seasonal and diurnal variations of cloud properties derived for CERES from VIRS and MODIS data, in *Proceedings of the 11th AMS Conference on Atmospheric Radiation*, pp. 20–23, Am. Meteorol. Soc., Boston, Mass.
- Minnis, P., L. Nguyen, D. R. Doelling, D. F. Young, W. F. Miller, and D. P. Kratz (2002b), Rapid calibration of operational and research meteorological satellite imagers, part II: Comparison of infrared channels, *J. Atmos. Oceanic Technol.*, 19, 1250–1266.
- Minnis, P., D. F. Young, S. Sun-Mack, P. W. Heck, D. R. Doelling, and Q. Z. Trepte (2003), CERES cloud property retrievals from imagers on TRMM, Terra, and Aqua, in *Proceedings of the SPIE 10th International Symposium on Remote Sensing: Conference on Remote Sensing of Clouds and the Atmosphere VII*, pp. 37–48, Int. Soc. for Opt. Eng., Bellingham, Wash.
- NOAA (1988), Digital relief of the surface of the Earth, *Data Announce. 88-MGG-02*, Natl. Geophys. Data Cent., Boulder, Colo. (available as <http://www.ngdc.noaa.gov/mgg/global/seltopo.html>)
- Paw, U. K. T., S. L. Ustin, and C.-A. Zhang (1989), Anisotropy of thermal infrared exitance in sunflower canopies, *Agric. Forest Meteorol.*, 48, 45–58.
- Prata, A. J. (1993), Land surface temperatures derived from AVHRR and ATSR I: Theory, *J. Geophys. Res.*, 89, 16,689–16,702.
- Suttles, J. T., R. N. Green, P. Minnis, G. L. Smith, W. F. Staylor, B. A. Wielicki, I. J. Walker, D. F. Young, V. R. Taylor, and L. L. Stowe (1988), Angular radiation models for Earth-atmosphere system, vol. I, Shortwave radiation, *NASA RP-1184*, 144 pp., NASA, Greenbelt, Md.
- Suttles, J. T., R. N. Green, G. L. Smith, B. A. Wielicki, I. J. Walker, V. R. Taylor, and L. L. Stowe (1989), Angular radiation models for Earth-atmosphere system, vol. 2, Longwave radiation, *NASA RP-1184*, 84 pp., NASA, Greenbelt, Md.
- Wielicki, B. A., B. R. Barkstrom, E. F. Harrison, R. B. Lee III, G. L. Smith, and J. E. Cooper (1996), Clouds and the Earth's Radiant Energy System (CERES): An Earth Observing System experiment, *Bull. Am. Meteorol. Soc.*, 77, 853–868.
- Wielicki, B. A., et al. (1998), Clouds and the Earth's Radiant Energy System (CERES): Algorithm overview, *IEEE Trans. Geosci. Remote Sens.*, 36, 1127–1141.

D. R. Doelling and A. V. Gambheer, Analytical Services and Materials, Inc., Hampton, VA 23666, USA. (d.doelling@larc.nasa.gov; a.v.gambheer@larc.nasa.gov)

P. Minnis, Atmospheric Sciences, NASA Langley Research Center, Hampton, VA 23681, USA. (p.minnis@larc.nasa.gov)